# Single step channeling in glass interior by femtosecond laser

Panjawat Kongsuwan, Hongliang Wang, and Y. Lawrence Yao

Citation: J. Appl. Phys. **112**, 023114 (2012); doi: 10.1063/1.4739304
View online: http://dx.doi.org/10.1063/1.4739304
View Table of Contents: http://jap.aip.org/resource/1/JAPIAU/v112/i2
Published by the American Institute of Physics.

# Single step channeling in glass interior by femtosecond laser

Panjawat Kongsuwan, Hongliang Wang, and Y. Lawrence Yao
*Department of Mechanical Engineering, Columbia University, New York, New York 10027, USA*

(Received 15 March 2012; accepted 27 June 2012; published online 25 July 2012)

Channeling inside a transparent material, glass, by femtosecond laser was performed by using a single step process rather than hybrid processes that combine the laser irradiation with an additional tool or step to remove the material. Tightly focusing of a single femtosecond laser pulse using proper optical and laser processing parameters could induce the micro-explosion and could create voids inside transparent materials, and the effects of these parameters on the resultant feature geometry and channel length were studied. Understanding of the channel length variation at different locations from the specimen surface could enhance prediction capability. Taking into account of the laser, material, and lens properties, numerical models were developed to predict the absorption volume shape and size at different focusing depths below the surface of a specimen. These models will also be validated with the variation in feature and channel lengths inside the specimen obtained from the experiments. Spacing between adjacent laser pulses and laser parameters was varied to investigate effects of channel overlapping and its influence on long channel formation. © *2012 American Institute of Physics*. [http://dx.doi.org/10.1063/1.4739304]

## I. INTRODUCTION

Microchannels are the essential features in micro-fluidic devices, micro-total analysis systems ($\mu$-TAS), and lab-on-a-chip (LOC) devices for biomedical applications. Lab-on-a-chip devices are microsystems integrated with functional components such as micro-optics, waveguides, and micro-fluidics aiming at the miniaturization onto a single substrate of several functionalities. LOCs use networks of microfluidic channels to transport, mix, separate, react, and analyze very small volumes of biological samples. Several substrate materials are used for LOC fabrication including silicon, glass, and polymers. However, glass is still the material of choice for many applications due to its chemical inert, stable in time, hydrophilic, nonporous, optically clear, and easily supports electro-osmotic flow.[1] Currently, fabrication of microfluidic devices still heavily relies on photolithographic techniques, which require multilayer and multistep processing procedures to form 3D microstructures.[2]

Femtosecond laser micromachining has emerged as a revolutionary technique for creating 3D microfluidic structures inside transparent substrates.[2] Laser irradiation inside transparent materials using the fluence equal or above the material damage threshold can alter the material structure and resulting mainly in positive/negative refractive index change. For higher fluence, a strong laser-matter interaction is occurred, and micro-explosion confined in the focal volume takes place with creation of voids. Glezer and Mazur[3] tightly focused femtosecond laser pulses to initiate micro-explosions inside transparent materials and found that submicrometer structures or voxels can be produced inside the materials. Juodkazis *et al.*[4] showed that the nanovoid in glass is formed as a result of shock and rarefaction waves at pulse power much lower than the threshold of self-focusing. Gamaly *et al.*[5] determined the mechanism of void formation as a result of micro-explosion and analyzed the size of the void as a function of the deposited energy. Using this mechanism, there is potential to form 3D patterns of voids inside glass.

Currently, there are mainly two strategies for fabricating 3D microchannels embedded in glass using femtosecond laser. The first strategy employs femtosecond laser direct writing followed by chemical etching in either silica glass or photosensitive glass. Marcinkevičius *et al.*[6] first demonstrated the possibility of 3D microchannel fabrication in fused silica using the combination of femtosecond laser dielectric modification and subsequent etching in an aqueous solution of hydrofluoric (HF) acid. Hnatovsky *et al.*[7] fabricated microchannels in fused silica and BK7 borosilicate glass by this two-step hybrid process, and also investigated the optimum irradiation conditions needed to produce high-aspect ratio microchannels with small symmetric cross-sections and smooth walls. Sun *et al.*[8] demonstrated the dependence of the microchannels fabricated in fused silica glass using chemical etching on the femtosecond laser pulses with different central wavelengths. Kiyama *et al.*[9] compared two different etching agents and demonstrated that a concentrated aqueous solution of potassium hydroxide (KOH) allowed higher etching selectivity than commonly used aqueous HF solution. Some researchers[10,11] also performed a three-step hybrid process to fabricate the 3D microfluidic structures by irradiating femtosecond laser into a photosensitive Foturan glass, thermal annealing to produce crystallites of lithium metasilicates in the laser-irradiated regions, and selectively chemical etching those regions in aqueous HF solution. Another strategy is to perform femtosecond laser drilling from the rear surface of the glass in contact with distilled water, by which the water introduced into the microchannel can help to remove the ablated material. Li *et al.*[12] first demonstrated the possibility of 3D microhole fabrication inside silica glass by water-assisted femtosecond laser drilling. Hwang *et al.*[13] fabricated straight, bent, and curved microfluidic channels in fused silica by this method, and

 

clarified that the debris is removed with the help of bubbles generated in the channel. Iga *et al.*[14] investigated how the diameters of the channels drilled from the rear surface of silica glass by a femtosecond laser depend on the incident energy and the number of laser pulses. An *et al.*[15] machined combined structures consisting of cascaded microchambers and microtrenches inside silica glass by water-assisted ablation with femtosecond laser pulses. The first process is limited by the etching selectivity as a function of etching period, and by the amount of fresh aqueous solution to reach the inward part of a microchannel. It thus usually gets a taper channel. For the second process, the ablated debris can no longer be ejected from the microchannel when the length of the channel increases. This clogging issue may be resolved by using a porous glass of which its porous network allows continuous infiltration of water into the ablation zone; however, the whole channel needs to be repeatedly scanned multiple times to completely remove all the debris, and subsequently post-annealing process is required to consolidate the porous glass into a compact glass resulting in shrinking of the channel dimensions in all directions.[2,16]

In this study, rather than using hybrid processes such as liquid assisted femtosecond laser processing or femtosecond laser irradiation combined with subsequently chemical etching the treated region, single-step channeling is investigated by attempting to connect the voids created from each single femtosecond laser pulse irradiation. This novel process uses single femtosecond laser pulses instead of pulse trains at a specific repetition rate and does not require an additional process to remove material from the channel. In order to understand the channel formation mechanism, to get the acceptable channel geometry, and to develop prediction capability, the effects of optical and laser parameters on the resultant morphology by single femtosecond laser pulse are studied. Numerical models are developed to predict the feature shape and lengths which also correspond to the channel lengths. The possibility of using the numerical features length simulated by absorption volume modeling and electromagnetic diffraction modeling as a guideline to estimate the experimental results is also discussed.

## II. BACKGROUND

### A. Channel formation and focusing effect

When a femtosecond laser pulse with high energy in the order of microjules is tightly focused into fused silica, nonlinear absorption will occur, a high number density of free electrons will be generated inside the absorption volume due to multi-photon and avalanche ionization. These hot free electrons will transfer their energy to ions, and thermal equilibrium of free electrons and lattice will be attained in picoseconds. In addition to a thermal process in which phase transitions take place, high pressure within the absorption volume builds up. When a high pressure and temperature volume are created inside this restricted volume, there is hydrodynamic expansion which proceeds as a micro-explosion. Shock wave emerges from this volume, compressing the surrounding material, and simultaneously rarefaction wave behind the shock front propagates in the opposite direction creating a void.[17,18]

Spherical aberration caused by focusing through the air-sample refractive index mismatched interface determined the variation of the threshold pulse energy as a function of the focusing depth and the size of the modified zones in fused silica.[19] Marcinkevičius *et al.*[20] reported that the spherical aberrations increased the size and distorted the shape of the photo-damaged region. Liu *et al.*[21] experimentally studied the influence of the focusing depth on both the index change threshold and damage threshold as well as on the cross section of the fabricated waveguides under irradiation of 1-kHz femtosecond laser pulses.

When the laser beam is focused through the air-glass interface, the paraxial focus or the focus produced by the central area of a focusing lens is located at the distance which is the product of the refractive index of glass and the focusing depth ($n_2 d$). By paraxial approximation and using the Snell's law on the interface, $n_2 \sin\theta_2 = n_1 \sin\theta_1 = NA$ is satisfied, and the longitudinal aberration range, $l_{pa}$, due to spherical aberration, which is the distance from the paraxial-ray focal plane to the peripheral-ray focal plane can be written as[21,22]

$$l_{pa} = \frac{\tan\theta_1}{\tan\theta_2} d - n_2 d = \left[ \sqrt{\frac{n_2^2 - NA^2}{1 - NA^2}} - n_2 \right] d, \qquad (1)$$

where $\theta_1$ is the incident angle of the focusing beam, $\theta_2$ is the refracted angle of the focusing beam, $n_2$ is the refractive index of glass, $d$ is the focusing depth from the interface, and $NA$ is the numerical aperture of an objective lens. On the other hand, by using diffraction theory and taking into account the variation in size of the converging Gaussian beam, $w(z) = w_0[1 + (\frac{\theta_z}{w_0})^2]^{1/2}$ is satisfied. The diffraction limited spot size location, $f$, will be related to the focusing depth, the converging incident angle, and the converging refracted angle as: $f = \frac{\theta_1 d}{\theta_2}$, and longitudinal aberration range, $l_{df}$, due to spherical aberration, which is the distance from the diffraction limited focal plane to the peripheral-ray focal plane can be written as

$$l_{df} = \frac{\tan\theta_1}{\tan\theta_2} d - \frac{\theta_1 d}{\sin^{-1}(\frac{NA}{n_2})} = \left[ \sqrt{\frac{n_2^2 - NA^2}{1 - NA^2}} - \frac{\sin^{-1}(NA)}{\sin^{-1}(NA/n_2)} \right] d. \qquad (2)$$

Either the longitudinal aberration range in Eq. (1) or that in Eq. (2) will have an influence on the nonlinear energy deposition by spreading the intensity distribution along its range. Therefore, the feature or the channel resulting from the laser-matter interaction region due to nonlinear absorption inside transparent materials will be proportional to the focusing depth.

### B. Numerical analysis

By taking into account the effect of the longitudinal aberration range, the numerical model based on the electromagnetic diffraction of a laser beam focused through an air-glass interface could be constructed to predict the absorption volume shape and size at different focusing depths below the surface of

a specimen. A laser beam of known power arrives at the interface through the first medium of refractive index $n_1$, and the interface at the surface of a specimen separates the medium of refractive index $n_1$ from the second medium of refractive index $n_2$. The electromagnetic field before the interface can be expressed as a superposition integral that sums up all possible plane waves propagating within the convergence angle of the high-aperture lens. Each plane wave is transmitted through the interface obeying the Fresnel refraction law. Using the fields calculated in the first medium as boundary conditions to obtain solution for the diffraction problem using a second integral representation of the electromagnetic field in the second medium. The resulting electric field distribution in the second medium is then a solution of the time-independent wave equation and Maxwell's equations and can be written as[23,24]

$$E_{2x}(x,y,z) = \frac{-ik_1 fl_0}{2}[I_0 + I_2\cos(2\theta_p)], \tag{3}$$

$$E_{2y}(x,y,z) = \frac{-ik_1 fl_0}{2} I_2 \sin(2\theta_p), \tag{4}$$

$$E_{2z}(x,y,z) = \frac{-ik_1 fl_0}{2} I_1 \cos\theta_p, \tag{5}$$

where $k_1$ is the wave number in the first medium, $f$ is the focusing distance, $l_0$ is the field amplitude factor, $x$ and $y$ are the positions in lateral directions, $z$ is the position in axial direction, and $\theta_p = \tan^{-1}(y/x)$ is the inclination angle. The integrals $I_0$, $I_1$, and $I_2$ are given by[23]

$$I_0 = \int_0^{\alpha} \sqrt{\cos\phi_1}\sin\phi_1 \exp[-id(k_1\cos\phi_1 - k_2\cos\phi_2)] \times (\tau_s + \tau_p\cos\phi_2) J_0(k_1\sqrt{x^2+y^2}\sin\phi_1) \times \exp(ik_2 z\cos\phi_2) d\phi_1, \tag{6}$$

$$I_1 = \int_0^{\alpha} \sqrt{\cos\phi_1}\sin\phi_1 \exp[-id(k_1\cos\phi_1 - k_2\cos\phi_2)] \times \tau_p \sin\phi_2 J_1(k_1\sqrt{x^2+y^2}\sin\phi_1)\exp(ik_2 z\cos\phi_2) d\phi_1 \tag{7}$$

$$I_2 = \int_0^{\alpha} \sqrt{\cos\phi_1}\sin\phi_1 \exp[-id(k_1\cos\phi_1 - k_2\cos\phi_2)] \times (\tau_s - \tau_p\cos\phi_2) J_2(k_1\sqrt{x^2+y^2}\sin\phi_1) \times \exp(ik_2 z\cos\phi_2) d\phi_1, \tag{8}$$

where $\alpha$ is the angular semi-aperture of the lens, $k_2$ is the wave number in the second medium, $\phi_1$ is the incident angle on the interface, $\phi_2$ is the refracted angle from the interface, $\tau_s$ and $\tau_p$ are the Fresnel coefficients, and $J_0$, $J_1$, and $J_2$ are the Bessel function of the first kind and order zero, one, and two, respectively. Hence, the distribution of the time-averaged electric energy density, $w_e$, and the total energy density, $w$, inside the specimen near the focal plane is the following:[24]

$$\langle w_e(x,y,z)\rangle = \frac{k_1^2 f^2 l_0^2}{64\pi}\{|I_0|^2 + 4|I_1|^2\cos^2\theta_p + |I_2|^2 + 2\cos(2\theta_p)\mathrm{Re}(I_0 I_2^*)\}, \tag{9}$$

$$\langle w(x,y,z)\rangle = \frac{k_1^2 f^2 l_0^2}{32\pi}\{|I_0|^2 + 2|I_1|^2 + |I_2|^2\}, \tag{10}$$

where * is the conjugate of a complex number. The electric energy density and total energy density of points in the vicinity of a focal plane will be significantly high, and when compared to the material damage threshold, the absorption volume could be identify to predict the size of features and channels at different focusing depths below the top surface of transparent materials.

## III. EXPERIMENTAL SETUP AND CHARACTERIZATION

Single step channeling is achieved by using a chirped amplified Ti:sapphire laser system which outputs high energy ultrashort pulses with 800 nm wavelength and 130 fs pulse duration at a 1 kHz repetition rate. The commercial grade S1-UV fused silica of 3.0 mm thick was cut to approximately 6 mm × 12 mm size. The laser beam was focused by 40x objective lens with numerical aperture (*NA*) 0.6 inside the specimen. A schematic diagram of the experimental setup is illustrated in Fig. 1. Different conditions of laser processing and optical parameters were applied by varying the energy of the laser pulses and focusing depth with respect to the top surface of the material. Long channels were obtained by cascading each channel generated by single laser pulses along an optical axis. Different laser pulse energies and focusing depth conditions were used to investigate the size of features and channels and to investigate the effects of channel overlapping and its influence on long channel formation.

After the femtosecond laser irradiation, transmission light differential interference contrast (DIC) optical microscopy was used to obtain the axial cross section (xz-plane) of the features and channels. The samples were ground and

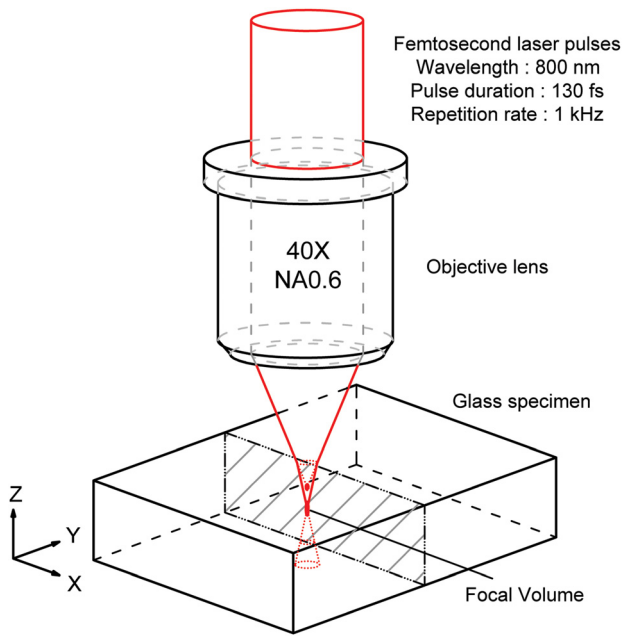


FIG. 1. Schematic illustration of experimental setup. The laser beam is focused through the air-glass interface into the interior of fused silica sample.

polished with lapping films to the line across channels. Reflection DIC optical microscopy and atomic force microscopy (AFM) topography were used to verify the existence of cavities on the polished surface. Raman spectroscopy was also carried out to further support whether the channels are real cavities.

## IV. RESULTS AND DISCUSSION

### A. Channel geometry

In order to achieve the long micro-scale channels in glass materials, other studies have used hybrid processes such as the combination of ultrashort laser irradiation and chemical etching or the liquid-assisted drilling by ultrashort laser scanning along an optical axis. However, single femtosecond laser pulse irradiation using high laser pulse energy and high numerical aperture of objective lens can also produce the reasonable long channels. Figure 2 shows the axial cross section (xz-plane) of features and channels created inside fused silica sample using laser pulse energy of 10 $\mu$J, 20 $\mu$J, and 30 $\mu$J, respectively, at the same focusing depth of 1500 $\mu$m below the top surface of 3 mm thick fused silica with standard flatness of 3–5 waves/in. from transmission DIC optical microscopy. The features defined by the distinctive color change around irradiated regions due to material alteration in optical and mechanical properties have high aspect ratios (length/width). The feature is strongly dependent on laser pulse energy as shown in Fig. 2, and the formation of larger features is corresponded to the higher the laser pulse energies. Inside the features, there are dark core regions, and these regions could be the consequence of the high level of interaction which subsequently generates high temperature and high pressure, and eventually causes the material explosion inside laser focal volume. The dark color regions are believed to be cavities, and the longest uniform dark color area inside the feature is identified as a channel from single laser pulse irradiation. The features and channels have a long and narrow tear drop shape corresponding to the shape of absorption volume.

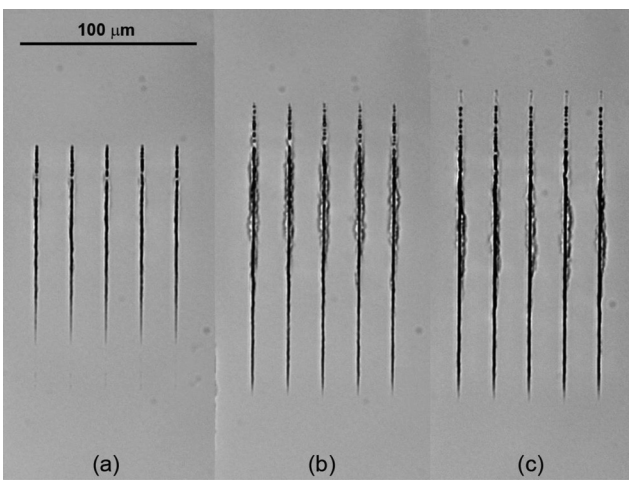


FIG. 2. Transmission DIC optical microscopy of axial cross section (xz-plane) of features and channels at same focusing depth of 1500 $\mu$m using pulse energy of (a) 10 $\mu$J, (b) 20 $\mu$J, and (c) 30 $\mu$J. The above three figures have been adjusted to the same scale.

To verify whether the identified channel is really a cavity, the fused silica sample was ground and polished from the top surface until the new polished surface was located at a line across channels. Figure 3 shows the radial cross section (xy-plane) of the polished sample irradiated by a series of single pulse with pulse energy of 30 $\mu$J from reflection DIC optical microscopy. From the reflective optical image in Fig. 3, the cross section of channels looks dark as well as the optical transmitted image, and the radial cross section shape of features and channels is irregular, roughly circular shape. The size of features and channels in this x-y view image is about a few micrometers corresponding well with the x-z view image. The cavity on the surface of transparent material normally looks dark when observed with the reflective optical microscope; therefore, these identified channels could be assumed as cavities as well. However, the AFM measurements of topography of channels in radial cross section were also performed to assure that the channels are cavities. The 3D topographic image of four distinctive channels with 10 $\mu$m spacing is illustrated in Fig. 4(a). The AFM top view image and line profiles across channels can also be seen in Fig. 4(b), and from the vertical line profile it can be concluded that the channel size in the direction perpendicular to the laser beam is about a few micrometers for laser pulse energy of 30 $\mu$J. In addition to the optical microscopy and AFM topography images, the Raman spectroscopy was also used to measure structural changes at and around the feature and channel inside the fused silica sample. Raman signal measurements were performed in a series of 15 points along the line cross the representative channel in x-z view as illustrated in Fig. 5(a). Raman spectral analysis of fused silica reveals that there are three-, four-, five-, and six-fold rings structure in the material, and these ring structures correspond to the 606 $cm^{-1}$, 495 $cm^{-1}$, and 440 $cm^{-1}$ peak in Raman spectra, respectively. The lowest peak intensity of all ring structures at point 10 which locates at center of the representative channel, and lower peak intensity at its adjacent points compared to other points in the reference region as plotted in Fig. 5(b) reply that there are low detected volumes of material in the vicinity of those points. This Raman results could be indirectly verified that the identified channels are cavities

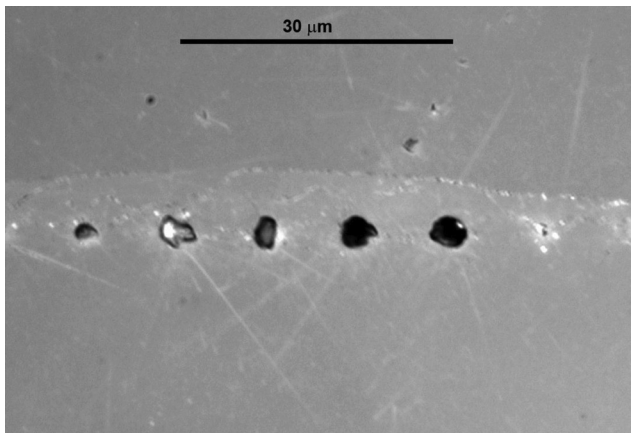


FIG. 3. Reflection DIC optical microscopy of radial cross section (xy-plane) of the new polished surface across the channels irradiated by a series of single pulse energy of 30 $\mu$J.

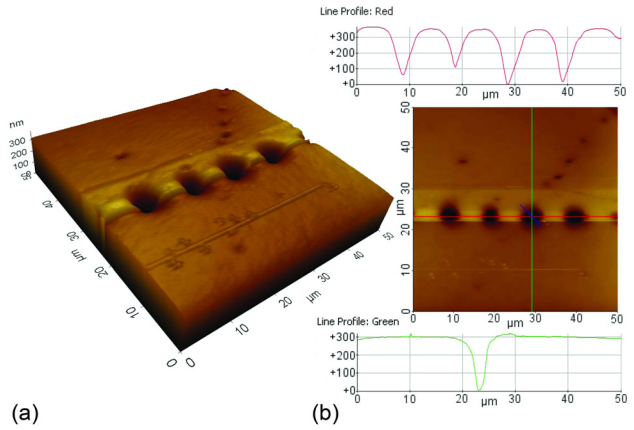


FIG. 4. (a) 3D AFM topography and (b) the AFM top view image and line profiles across the channels on the new polished surface (xy-plane) across the channels irradiated by a series of single pulse energy of 30 $\mu$J.

as well. Therefore, the optical microscopy, AFM topography, and Raman spectroscopy support each other that the defined channels are cavities. Sidewall surface roughness is an important parameter in fluid flow through microchannels for optofluidic applications. Although it is not focused in this study, and the spatial resolution of the measurement with respect to the size of microchannels may not be high, inspection on the cross section of microchannels using optical profilometer suggested a sidewall surface roughness of $\sim$1 nm.

Figure 6 shows the shape and size of features and channels created inside fused silica sample using same laser pulse energy of 30 $\mu$J at different focusing depths in the range of 500–2500 $\mu$m below the top surface within 3 mm thick of the material from the x-z view. It can be seen that the size especially in the optical direction (z-axis) is strongly dependent on the focusing depth. The greater the focusing depths correspond to the generation of longer features and channels. The variation in size in the optical direction is caused by spherical aberration due to the focusing of laser beam through the refractive index mismatched air-glass interface. On the one hand, as illustrated in Fig. 1, the plane of focal volume will move to the lower location than the Gaussian focus plane (if there is no interface) due to the refraction of laser beam. On the other hand, due to the presence of the air-glass interface,

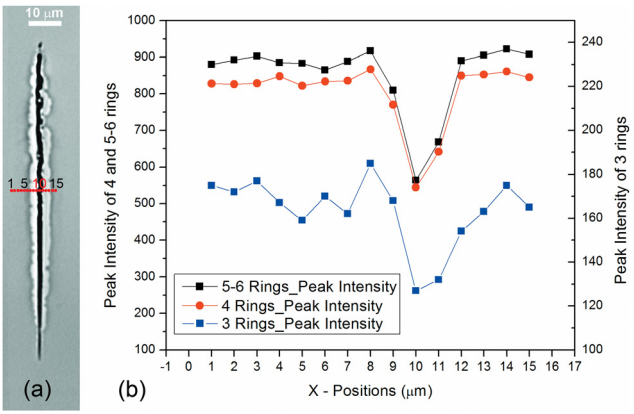


FIG. 5. (a) Raman signal measurements points across the axial cross section (xz-plane) of a feature and channel, and (b) the peak intensity of the 3–6 rings structure of 15 points across the channel.

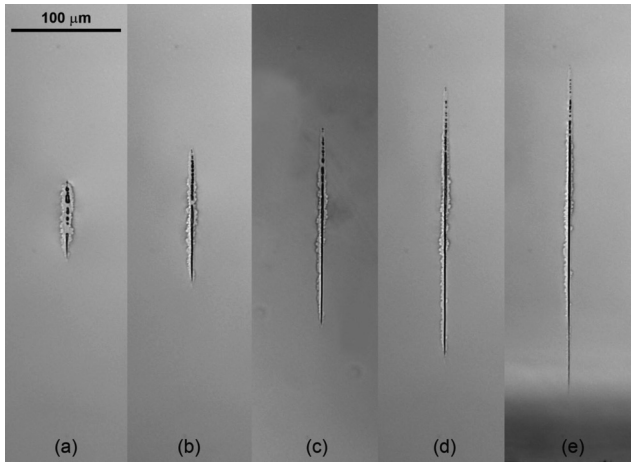


FIG. 6. Transmission DIC optical microscopy of axial cross section (xz-plane) of features and channels using same pulse energy of 30 $\mu$J at different focusing depths of (a) 500 $\mu$m, (b) 1000 $\mu$m, (c) 1500 $\mu$m, (d) 2000 $\mu$m, and (e) 3000 $\mu$m. The above five figures have been adjusted to the same scale.

the focused rays inside laser beam cone, which initially converge to the single focal plane at different angles, will diversely propagate to different focal planes in glass, and this phenomenon results in a longitudinal aberration range. The deeper the focusing depths will correspond to the occurrence of longer aberration ranges. Fig. 7 shows the effect of material surface roughness on the feature lengths using same laser pulse energy of 30 $\mu$J at different focusing depths. The size of features generated by focusing the laser beam through the optical finishing smooth surface with standard flatness of 3–5 waves/in. is significantly enhanced from the case that generated by focusing through the rough cutting surface using speed saw. With optical finishing smooth surface, low fraction of laser beam reflection and scattering on the surface is occurred, and higher energy can be deposited inside the transparent material. Therefore, to generate quite reasonable long features and channels inside fused silica by single

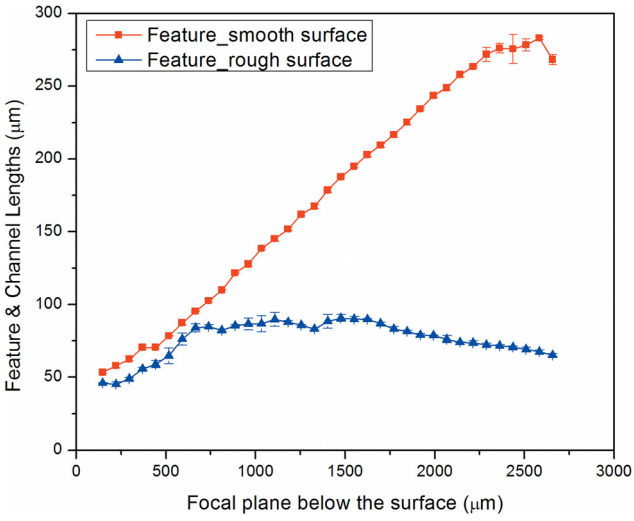


FIG. 7. The effect of material surface roughness on the feature lengths using same laser pulse energy of 30 $\mu$J at different focusing depths. Error bars denote standard deviation.

femtosecond laser pulse, one should seriously consider using the optical finishing smooth top surface of the material.

Figure 8 shows the feature lengths at different focusing depths of pulse energies of 10 $\mu$J, 20 $\mu$J, and 30 $\mu$J, respectively, compared to longitudinal aberration ranges in Eq. (1) defined as paraxial aberration ranges in Sec. II A. The feature lengths have increasing trends with the focusing depths with respect to the top surface of samples and range from 23 to 283 $\mu$m in length and 4 to 46 in aspect ratio. As seen in Fig. 8, the feature lengths depend on both focusing depths and laser pulse energies. The greater the focusing depth, the longer the feature length; the length of the feature also increases with laser pulse energy. The features' lengths of all pulse energies in this study fall within the paraxial aberration ranges. This could be due to the deposited laser pulse energy will be absorbed and broadly distributed in this paraxial aberration ranges, and the absorbed energy density of points only within this ranges will probably be greater than the material damage threshold. It results in feature lengths shorter than the paraxial aberration ranges. The feature lengths show leveling trends at deep focusing depths, and due to the spreading of lower energy within the same aberration ranges caused by the lower absorbed energy density, the lower pulse energies level off at shallower focusing depths compared to the higher ones as observed in Fig. 8. Although the paraxial aberration ranges are not perfectly matched the feature lengths, a guideline that the feature lengths will be approximately equal or less than the paraxial aberration ranges could be used.

Figure 9 shows the channel lengths at different focusing depths of pulse energies of 10 $\mu$J, 20 $\mu$J, and 30 $\mu$J, respectively, compared to longitudinal aberration ranges in Eq. (2) defined as diffraction limited aberration ranges in Sec. II A. In the range of this study with respect to focusing depths, the channel lengths have only an increasing trend for the case of 30 $\mu$J pulse energy but also show leveling and decreasing trends for the case of 10 $\mu$J pulse energy. It replies that at further depth locations the pulse energy will be over spreading such that the absorbed energy density that is greater than the material damage threshold occurs in shorter and shorter

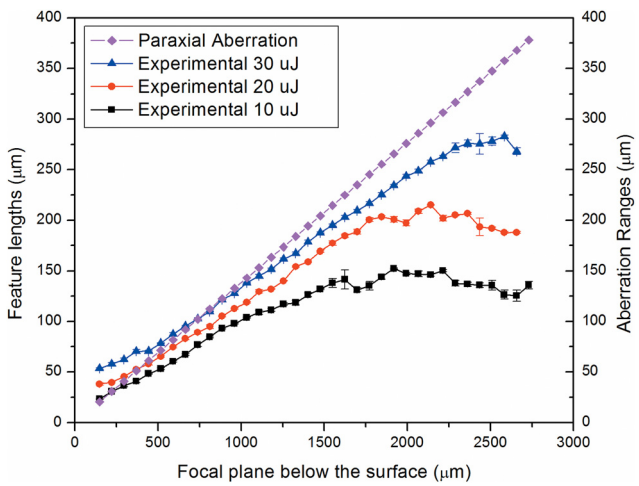


FIG. 8. Comparison of experimental feature lengths at 10 $\mu$J, 20 $\mu$J, and 30 $\mu$J, and the paraxial aberration ranges at different focusing depths. Error bars denote standard deviation.

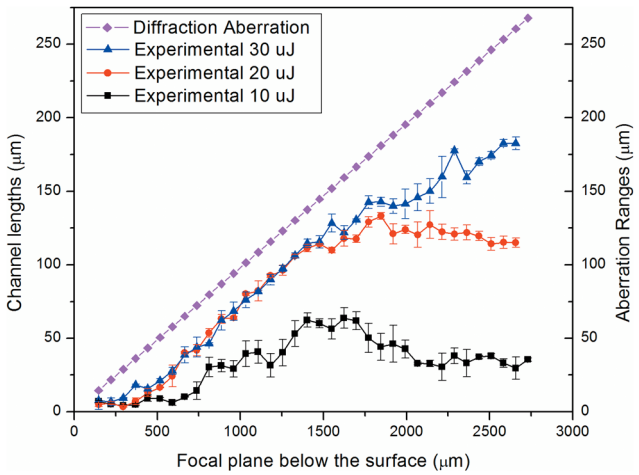


FIG. 9. Comparison of experimental channel lengths at 10 $\mu$J, 20 $\mu$J, and 30 $\mu$J, and the diffraction limited aberration ranges at different focusing depths. Error bars denote standard deviation.

ranges, and the material explosion will happen in shorter ranges as well resulting in shorter channel lengths as clearly seen in case of 10 $\mu$J in Fig. 9. The diffraction limited aberration ranges are sometimes shorter or longer than the feature lengths at different laser pulse energies in this study; however, they are quite close to and always greater than the channel lengths of all pulse energies and focusing depths. Therefore, a quick guideline could also be used to estimate that the resulting channel lengths will be less than the diffraction limited aberration ranges.

By cascading a single pulse channel along the optical axis within the thickness of fused silica sample using a long working distance objective lens, the connection of channels can be performed to produce a long channel which has adequate length for most microfluidic and lab-on-a-chip applications. However, the appropriate overlapping distance of single channel has to be considered. Figures 10(a) and

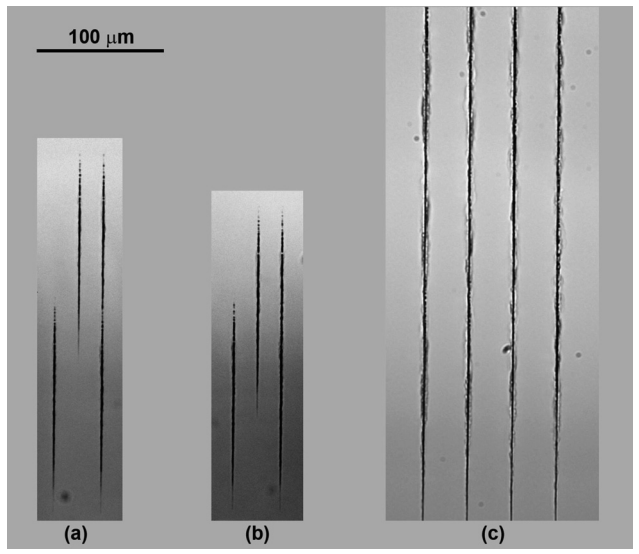


FIG. 10. Cascading of two single pulses with (a) an inadequate overlapping distance, and (b) an appropriate overlapping distance. (c) Cascading of multiple single pulses using pulse energy of 30 $\mu$J. The above three figures have been adjusted to the same scale.

10(b) show the transmission DIC optical image in xz-plane of cascading channels using different overlapping distances for two single pulses. The left and the middle one are the locations of the bottom and the top channels that will be cascading, respectively. The right channels are the results of cascaded channels. As seen in Fig. 10(a), the two channels are not completely connected due to an inadequate overlapping distance. When the overlapping distance is increased, the cascaded channel has uniform dark color in the overlapping region, which implies that the channel cascading can be succeeded if an appropriate overlapping distance has been used. Figure 10(c) shows the representative cascaded channels of multiple single pulses. From observation by optical microscope, the channel cascading is usually succeeded if the overlapping distance of the features is equal to or greater than 68%. Although the microchannels by single-step channeling process can be performed only in the direction that is paralleled to the incident laser beam, and the shape of microchannels has to be simple and straight rather than contour or complex, this novel process could still be a potential alternative to produce micro-scale channels inside transparent materials for microfluidic and lab-on-a-chip applications. In addition to long 1D channel, which is easily fabricated by this technique, the 2D and 3D structures with the changes in directions of microchannels could be fabricated by changing the setups during processing or by using a robot arm with six degrees of freedom to handle the workpiece. However, the effects of non-perpendicular surface with respect to the incident laser beam on shape and size of microchannels need to be further explored.

## B. Numerical modeling

From experimental results, the shape and size of features and channels vary as a function of focusing depth. In order to predict the shape and size of those features and channels at different focusing depths below the specimen surface, the two numerical models of laser absorption volume and electric energy density field inside a transparent material were constructed. The first numerical model considers the temporal profile and spatial intensity of Gaussian laser beam which propagates through a focusing lens and an air-glass interface to points in the vicinity of a focal plane and determines breakdown points which have intensity greater than the material intensity damage threshold. The second numerical model considers the electric field inside the second medium after focusing electromagnetic wave through a focusing lens and an interface between two different mediums, then determines the electric energy density field in the vicinity of a focal plane, and compares it with the energy density damage threshold of the material. Both numerical models will take effect of the longitudinal aberration ranges into account.

### 1. Absorption volume modeling

From temporal and spatial distribution characteristics of femtosecond laser pulses, the intensity of an unfocused laser beam in each time slice was determined. When the unfocused laser beam has been converged to the smaller area in the vicinity of a focal plane, the magnified intensity will be compared to the material intensity damage threshold, and the breakdown points which have intensity greater than the threshold will be determined.[25] Consequently, the corresponding locations in the optical axis of these breakdown points will be calculated considering focusing parameters, optical properties of two materials, and aberration effects from air-glass interface. Eventually, all breakdown points will combine and generate the absorption volume. Figure 11 shows the representative simulated axial cross section (rz-plane) of the absorption volume by 30 $\mu$J pulse energy at the focusing depth (a paraxial focal plane) of 1000 $\mu$m below the top surface of fused silica material. The cross section shape of the absorption volume looks like the teardrop shape and has high aspect ratios (length/width). It is interesting that the top breakdown point in optical axis of this representative absorption volume is occurred closely to the diffraction limited focal plane at $-1040.4$ $\mu$m rather than the paraxial focal plane at $-1000$ $\mu$m. The size of the absorption volume is indeed dependent on the focusing depths and laser pulse energies, and the longest distance along the optical axis of the absorption volume is defined as the numerical feature lengths simulated by the absorption volume modeling. More details of the results from this numerical model will be shown and verified with the other numerical model and the experimental results in Sec. IV B 3.

### 2. Electromagnetic diffraction modeling

A superposition of plane waves inside mediums can represent electromagnetic fields. Taking into account the optical properties of two different mediums, the focusing parameters, and Fresnel's refraction law at the interface between two different mediums, a superposition of refracted plane waves can construct the time-independent or time-averaged electric and magnetic fields. The area in the vicinity of the focal plane which has high enough electric energy density especially greater than the damage threshold of the material can be counted as a material structural alteration area which represents the feature and channel generated by a single femtosecond laser pulse. Figure 12 illustrates the 3D surface

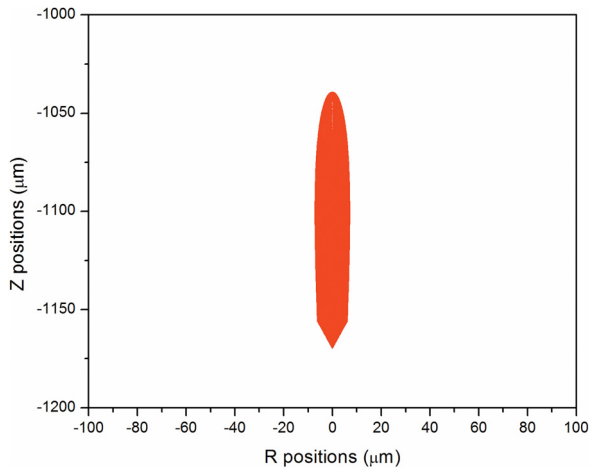


FIG. 11. The representative simulated cross section (rz-plane) of the absorption volume by 30 $\mu$J pulse energy at the focusing depth of 1000 $\mu$m from the absorption volume model.

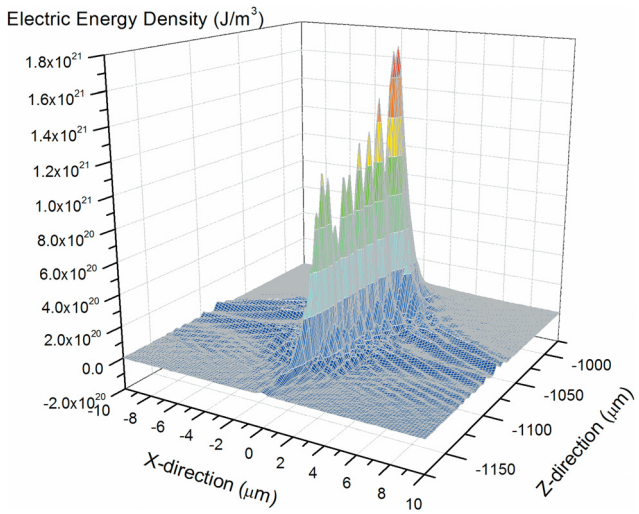


FIG. 12. The 3D surface map of representative electric energy density field on the xz-plane along an optical axis in the vicinity of the focal plane for laser pulse energy of 30 $\mu$J at the focusing depth of 1000 $\mu$m.

map of representative electric energy density field on the xz-plane along an optical axis in the vicinity of the focal plane for laser pulse energy of 30 $\mu$J at the focusing depth of 1000 $\mu$m below the top surface of fused silica material. The region of interest is located between the focal plane of axial and peripheral rays within the angular semi-aperture of the objective lens with NA = 0.6. As seen in Fig. 12, the electric energy density is extremely high only near the optical axis between the paraxial focal plane at $-1000$ $\mu$m and the peripheral focal plane at $-1138.4$ $\mu$m below the top surface of the material.

The contour map of electric energy density in this region of interest by 30 $\mu$J pulse energy at 1000 $\mu$m focusing depth is shown in Fig. 13. This contour looks like tear drop shape and similar to the appearance of features and channels, and the total length and width of this contour are also about the same size as the experimental features in Fig. 6(b). In Fig. 13, lines C1, C2, C3, C4, and A1 represent section lines across this representative high electric energy density field. Lines C1 and C4 are located along the paraxial- and peripheral-ray focal planes, respectively. Lines C2 and C3 are located along the top two peaks of electric energy density, and line A1 is located along the optical axis. The contour and 3D surface maps on xy-planes along lines C1, C2, C3, and C4 are illustrated in Figs. 14(a)–14(d), respectively. From these contour and 3D surface maps, the distribution of electric energy density along axes perpendicular to the laser propagation direction has a Gaussian profile. The peak energy density of electric field on both paraxial- and peripheral-ray focal planes in Figs. 14(a) and 14(d) is slightly less than the material damage threshold, and this could give the answer why the experimental feature lengths in Sec. IV A are usually shorter than the defined paraxial aberration. The contour maps in Figs. 14(b) and 14(c) along the xy-planes which have top two peaks of electric energy density show multiple rings which have energy density greater than the material damage threshold. The size of outbound rings with such high electric energy density is approximately 2 $\mu$m, and it can be seen that this size is corresponded to the width of experimental features and channels in Sec. IV A. Figure 15 shows the electric energy density on the optical axis along line A1 in Fig. 13. The oscillation of the electric energy density along this optical axis could be due to the constructive and destructive interference of phase factor resulting from a superposition of refracted plane waves. From the line profile of electric energy density along the optical axis, the numerical feature length simulated by the electromagnetic diffraction model is defined as the distance, whereas the electric energy density is greater than the material damage threshold ($E_{th}$) as illustrated in Fig. 15. The numerical feature lengths from this model are strongly dependent on both the focusing depths and the laser pulse energies. More details of the results from this numerical model will be shown and verified with the previous numerical model and the experimental results in Sec. IV B 3.

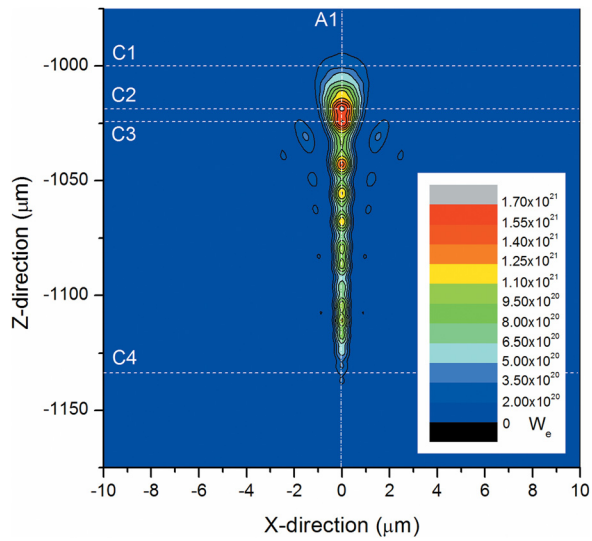


FIG. 13. The contour map of representative electric energy density field on the xz-plane along an optical axis in the vicinity of the focal plane for laser pulse energy of 30 $\mu$J at the focusing depth of 1000 $\mu$m. Lines C1, C2, C3, C4, and A1 represent section lines across this field.

### 3. Validation of numerical models with experimental results

From the simulated absorption volumes similar to the representative cross section map in Fig. 11, and the simulated electric energy density line profiles along the optical axis similar to the representative profile in Fig. 15, the numerical feature lengths calculated by absorption volume and electromagnetic diffraction models at different focusing depths below the top surface of fused silica sample using the single femtosecond laser pulse energy of 30 $\mu$J as well as the experimental feature lengths are plotted in Fig. 16. The feature lengths from both numerical models have increasing trends with the focusing depths, and line up pretty well with the experimental feature length results. Especially for this particular laser pulse energy of 30 $\mu$J, the results from the electromagnetic diffraction model almost perfectly match the experimental results and better predict the feature lengths than the absorption volume modeling. By taking the

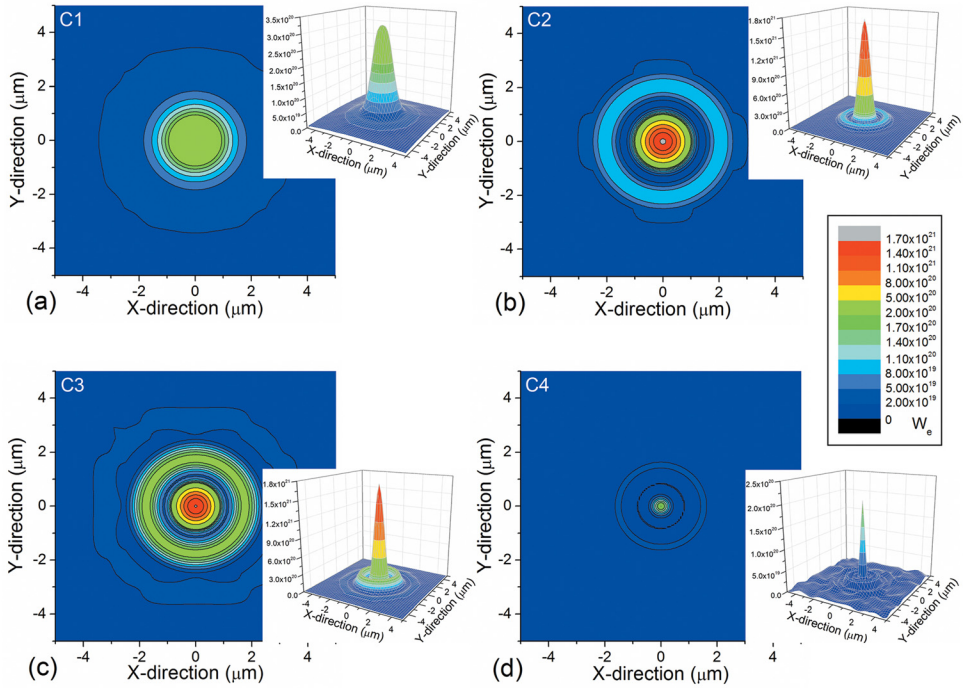


FIG. 14. The contour and 3D surface maps in xy-planes along (a) line C1 located along the paraxial-ray focal plane, (b) line C2 located along the highest peak of electric energy density, (c) line C3 located along the second highest peak of electric energy density, and (d) line C4 located along the peripheral-ray focal plane.

aberration effect from air-glass interface into consideration, the locations of breakdown points in the optical axis of the absorption volume model are approximated by using the law of tangents; therefore, the longer the focusing depth, the greater the discrepancy predicted by the absorption volume model. The electromagnetic diffraction model thus gives the better fit for the focusing depth longer than 500 $\mu$m. For the focusing depth shorter than 500 $\mu$m, there is less spreading of the electric energy density near focal plane, and energy density could be so intensified that it would conduct to an adjacent area resulting in longer experimental feature length; therefore, the absorption volume model apparently gives better results. Figure 17 shows the numerical and experimental feature length as a function of laser pulse energy at two different focusing depths of 1000 $\mu$m and 1500 $\mu$m below the top surface of fused silica sample, respectively. As seen in Fig. 17, the electromagnetic diffraction model has some difficulties in determining the feature length when the laser pulse energy is less than 20 $\mu$J due to the electric energy density become lower than the material damage threshold at low pulse energies, and the level of laser pulse energy at which feature lengths could not be defined is also dependent on the focusing depths. The deeper the focusing depths, the greater the spreading of electric energy density resulting in the higher levels of pulse energy at which the feature lengths could not be determined. This problem could be due to the time-independent or time-averaged based approximation of the model whereas the absorption volume model which considers the temporal profile of laser pulse as well as the spatial profile still be able to predict the feature lengths at low pulse energy, however, the discrepancy between the numerical and experimental results will increase correspond to the lower pulse energies. Therefore, depending on the working

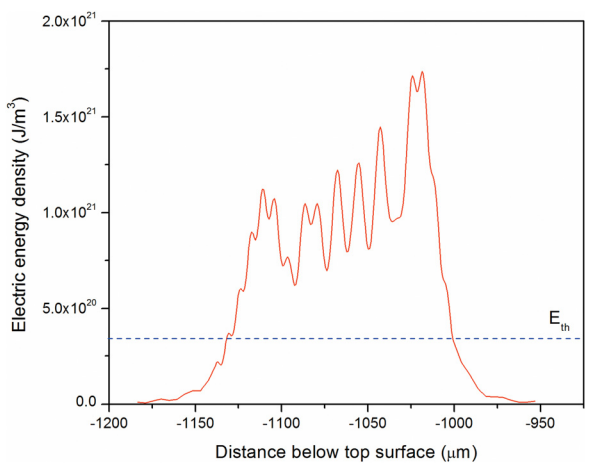


FIG. 15. The electric energy density on the optical axis along line A1 in Fig. 13 compared to the damage threshold of fused silica sample.

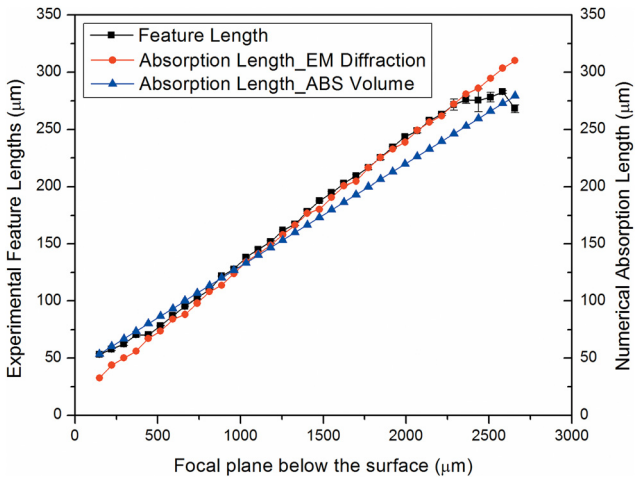


FIG. 16. Comparison of feature lengths from two numerical models and experimental results at different focusing depths using laser pulse energy of 30 $\mu$J.

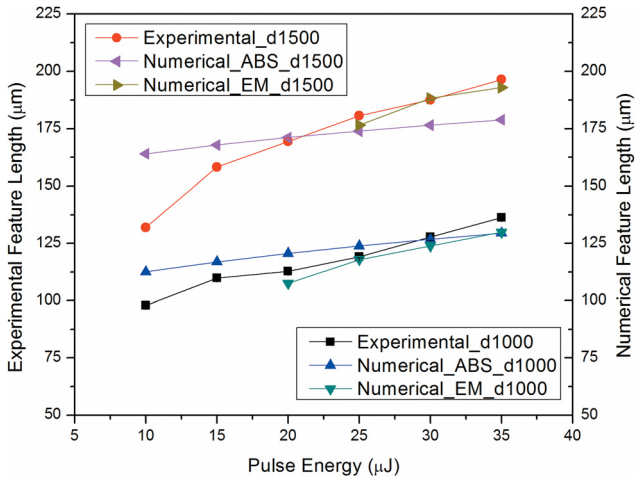


FIG. 17. Comparison of feature lengths from two numerical models and experimental results at different pulse energies for focusing depth of 1000 $\mu$m and 1500 $\mu$m below the top surface of fused silica sample, respectively.

parameters, the electromagnetic diffraction model better predicts the feature lengths with some restrictions at low pulse energies.

## V. CONCLUSION

Single step channeling inside fused silica glass was performed by a series of single femtosecond laser pulses. The axial cross section of the generated features by the transmission DIC optical microscopy revealed that they range from 23 to 283 $\mu$m in length and 4 to 46 in aspect ratio. Those features also have a long uniform dark colored region, which is identified as a microchannel. The radial cross sectioning of this channel in conjunction with the surface topography confirmed that the channels are cavities. The reflection DIC optical microscopy and Raman spectroscopy also support this fact. The size of the features and channels is strongly dependent on the laser pulse energies and focusing depths. The variation in size of features and channels with focusing depths is due to aberration caused by the refractive index mismatch at air-glass interface. With overlapping distance of the feature equal or greater than 68%, channel cascading could be successfully performed to produce a longer channel in millimeter scale. Two numerical models were developed to investigate the shape and size of features and channels generated by single femtosecond laser pulses at different laser pulse energies and focusing depths. The numerical results were validated using the experimental ones, and both absorption volume and electromagnetic diffraction models could be used to estimate the feature lengths.

## ACKNOWLEDGMENTS

This work is partially supported under NSF Grant No. CMMI-0936171. Financial support from the Royal Thai government is also gratefully acknowledged. Research carried out in part at the Center for Functional Nanomaterials, Brookhaven National Laboratory, which is supported by the U.S. Department of Energy, Office of Basic Energy Sciences, under Contract No. DE-AC02-98CH10886.

[1]R. Osellame, H. J. W. M. Hoekstra, G. Cerullo, and M. Pollnau, Laser Photonics Rev. **5**, 442–463 (2011).
[2]Y. Liao, Y. Ju, L. Zhang, F. He, Q. Zhang, Y. Shen, D. Chen, Y. Cheng, Z. Xu, K. Sugioka, and K. Midorikawa, Opt. Lett. **35**, 3225–3227 (2010).
[3]E. N. Glezer and E. Mazur, Appl. Phys. Lett. **71**, 882 (1997).
[4]S. Juodkazis, H. Misawa, T. Hashimoto, E. G. Gamaly, and B. Luther-Davies, Appl. Phys. Lett. **88**, 201909 (2006).
[5]E. Gamaly, S. Juodkazis, H. Misawa, B. Lutherdavies, A. Rode, L. Hallo, P. Nicolai, and V. Tikhonchuk, Curr. Appl. Phys. **8**, 412–415 (2008).
[6]A. Marcinkevičius, S. Juodkazis, M. Watanabe, M. Miwa, S. Matsuo, H. Misawa, and J. Nishii, Opt. Lett. **26**, 277 (2001).
[7]C. Hnatovsky, R. S. Taylor, E. Simova, P. P. Rajeev, D. M. Rayner, V. R. Bhardwaj, and P. B. Corkum, Appl. Phys. A **84**, 47–61 (2006).
[8]Q. Sun, A. Saliminia, F. Théberge, R. Vallée, and S. L. Chin, J. Micromech. Microeng. **18**, 035039 (2008).
[9]S. Kiyama, S. Matsuo, S. Hashimoto, and Y. Morihira, J. Phys. Chem. C **113**, 11560–11566 (2009).
[10]K. Sugioka, Y. Cheng, and K. Midorikawa, Appl. Phys. A **81**, 1–10 (2005).
[11]Z. Wang and H. Zheng, Laser Part. Beams **27**, 521–528 (2009).
[12]Y. Li, K. Itoh, W. Watanabe, K. Yamada, D. Kuroda, J. Nishii, and Y. Jiang, Opt. Lett. **26**, 1912 (2001).
[13]D. J. Hwang, T. Y. Choi, and C. P. Grigoropoulos, Appl. Phys. A: Mater. Sci. Process. **79**, 605–612 (2004).
[14]Y. Iga, T. Ishizuka, W. Watanabe, K. Itoh, Y. Li, and J. Nishii, Jpn. J. Appl. Phys., Part 1 **43**, 4207–4211 (2004).
[15]R. An, Y. Li, Y. Dou, D. Liu, H. Yang, and Q. Gong, Appl. Phys. A **83**, 27–29 (2006).
[16]Y. Liao, J. Song, E. Li, Y. Luo, Y. Shen, D. Chen, Y. Cheng, Z. Xu, K. Sugioka, and K. Midorikawa, Lab Chip **12**, 746–749 (2012).
[17]E. G. Gamaly, B. Luther-Davies, L. Hallo, P. Nicolai, and V. T. Tikhonchuk, Phys. Rev. B **73**, 214101 (2006).
[18]L. Hallo, C. Mézel, A. Bourgeade, D. Hébert, E. G. Gamaly, and S. Juodkazis, *in Extreme Photonics & Applications*, edited by T. J. Hall, S. V. Gaponenko, and S. A. Paredes (Springer, The Netherlands, 2010), pp. 121–146.
[19]C. Hnatovsky, R. S. Taylor, E. Simova, V. R. Bhardwaj, D. M. Rayner, and P. B. Corkum, J. Appl. Phys. **98**, 013517 (2005).
[20]A. Marcinkevičius, V. Mizeikis, S. Juodkazis, S. Matsuo, and H. Misawa, Appl. Phys. A: Mater. Sci. Process. **76**, 257–260 (2003).
[21]D. Liu, Y. Li, R. An, Y. Dou, H. Yang, and Q. Gong, Appl. Phys. A **84**, 257–260 (2006).
[22]Q. Sun, H. Jiang, Y. Liu, Y. Zhou, H. Yang, and Q. Gong, J. Opt. A, Pure Appl. Opt. **7**, 655–659 (2005).
[23]P. Török, P. Varga, Z. Laczik, and G. R. Booker, J. Opt. Soc. Am. A **12**, 325 (1995).
[24]B. Richards and E. Wolf, Proc. R. Soc. London, Ser. A **253**, 358–379 (1959).
[25]P. Kongsuwan, G. Satoh, and Y. L. Yao, J. Manuf. Sci. Eng. **134**, 011004 (2012).